

# Chapter 4

## Diffusion Barriers

### 4.1 Chapter Summary

The focus of the experiments described in this chapter is to address the effects on vapor transport of various physical barriers which are more complex than homogeneous porous media. The diffusion coefficient of water vapor is measured at conditions appropriate to the surface of Mars for a variety of particle size mixtures and soil compositions. The work of *Hudson et al. (2007)* (Chapter 3) on the diffusivity,  $D$ , of dusts (*i.e.*, particles with mean sizes  $< 10 \mu\text{m}$ ) is extended. Mixtures of two dusts types with larger particles (50–80  $\mu\text{m}$  glass beads) are studied and the effect of varying dust content on  $D$  is discussed. Chemically cemented duricrusts are simulated with magnesium sulfate encrusted glass beads, and a range of salt contents are examined.

The environmental chamber and instrumental setup are identical to that described in *Hudson et al. (2007)* and Section 3.2 in all but two respects. (1) The freezer temperature was reduced to give ambient chamber temperatures of  $\sim 250 \text{ K}$  rather than  $\sim 263 \text{ K}$ . (2) Pressure is now maintained more accurately with active PID control of an STEC-4400 mass flow controller via an USB-1408FS datalogger from Measurement Computing Corporation. A schematic of the experimental setup is in Figure 3.1. As before, data for calculating diffusion coefficients are taken from the stable interval following the decay of initial transients.

Most unconsolidated mixtures were not actively compressed, but may be subject to self-compression. In most cases, the sample surfaces remain within 1 mm of the caddy top despite sublimation of the ice on which they rest. Some samples with very high dust fractions exhibit some settling as the container is moved from the preparation station to the vacuum chamber. This amounts to about 12% of the 5 cm sample depth, at most. The reduced thickness is measured and included in subsequent calculations; additional material is not added.

It is found that the value of the diffusion coefficient can be reduced by up to a factor of 10 for heavily salt-encrusted soils, with the minimum observed  $D$  being  $0.4 \pm 0.04 \text{ cm}^2 \text{ s}^{-1}$ . Moderate amounts of salt only produce minor reductions in  $D$ . Mechanical packing of pure dusts can lower  $D$

by a similar amount, while mixtures including a portion of sand-sized particles produce at most a factor of  $\sim 4$  reduction.

This work indicates that present-day processes of aeolian redistribution, moderate levels of salt encrustation, and volatile loss from dirty ice would be inefficient at producing soil deposits and lags on Mars that pose significant barriers to diffusion. Therefore, subsurface ice deposits that are thermally unstable would not be protected against sublimative loss by such materials.

## 4.2 Materials

A variety of materials have been used to explore the effects of particle size distribution and salt crust formation on diffusion coefficients in simulated Mars soils. Properties of glass beads, crushed JSC Mars-1 dust, and 1–3 micron dust are described in Section 3.3. Figure 3.4 shows optical micrographs of the simulants at the same scale. Further description of preparation methods used for mixtures and salt crusts are presented here. Prior to use, all samples are dried in an oven at 383 K and then stored in air-tight containers.

Geometric porosities of the separate materials were determined by weighing a known volume of bulk sample to determine a bulk density,  $\rho_{\text{bulk}}$ , and ratioing this against the known specific gravity of the individual particles ( $\phi = 1 - \rho_{\text{bulk}}/\rho_{\text{true}}$ ). The results are given in Table 3.1.

### 4.2.1 Mixtures

Throughout this work, “Mixture Type 1” will refer to mixtures of crushed JSC Mars-1 material and 50–80  $\mu\text{m}$  glass beads. “Mixture Type 2” will refer to mixtures of 1–3  $\mu\text{m}$  silica dust and glass beads.

To study the effect of bimodal particle distributions, particularly the effect of included dust in a deposit of sand-sized particles, six mixtures (A through F) of silica-glass beads (nominal diameter 50–80  $\mu\text{m}$ ) and either crushed JSC Mars-1 or 1–3  $\mu\text{m}$  dust were prepared. The mixtures, both in terms of mass fraction of fines ( $X_f = M_f/(M_f + M_c)$ ) and mass ratio of fines to coarse material ( $M_f/M_c$ ) are shown in Table 4.1. Volume fraction of dust is an indeterminate quantity since  $\phi$  and  $\rho_{\text{bulk}}$  for the fine materials can vary over a large range depending on the degree of compaction in the mixture; it is therefore not used to describe the mixtures.

The porosity of the mixtures may be estimated by first calculating the fraction of the volume occupied by each component. Given a measurement of total mixture volume  $V_T$  and mixture mass  $M_T$ , the volume fraction of each are  $v_f = (M_f/V_T)(1/\rho_{f,\text{true}})$ , and  $v_c = (M_c/V_T)(1/\rho_{c,\text{true}})$ , where  $M_f$  and  $M_c$  are the masses of the fine and coarse components as calculated from  $M_f = X_f M_T$  and  $M_c = (1 - X_f)M_T$ . The free volume is then the sum of these volume fractions subtracted from

	A	B	C	D	E	F
Mixture Type 1						
$X_f(\%)$	43.1	27.4	15.9	11.4	7.06	3.29
$M_f/M_c(\%)$	75.6	37.8	18.9	12.9	7.56	3.40
$\rho_{\text{mix}}, (\text{g cm}^{-3})$	2.72	2.63	2.58	2.55	2.53	2.52
Mixture Type 2						
$X_f(\%)$	39.8	24.9	14.2	10.1	6.19	2.82
$M_f/M_c(\%)$	66.0	33.1	16.6	11.2	6.60	2.90
$\rho_{\text{mix}}, (\text{g cm}^{-3})$	2.56	2.54	2.52	2.51	2.51	2.50

Table 4.1: Porosities of mixtures with glass beads

unity:

$$\phi_{\text{mix}} = 1 - \frac{M_T}{V_T} \left[ \frac{X_f}{\rho_{f,\text{true}}} + \frac{(1 - X_f)}{\rho_{c,\text{true}}} \right]. \quad (4.1)$$

Here,  $\rho_{\text{mix}}$  is determined as proxy for the true density of the mixture if it were composed of a homogeneous granular component, thus:  $\rho_{\text{mix}}^{-1} = X_f/\rho_{f,\text{true}} + (1 - X_f)/\rho_{c,\text{true}}$ . These values are also given in Table 4.1. Individual porosities are determined for each simulant and are tabulated in the auxiliary material.

The amount of dust included in a mixture may, in addition to its mass fraction of the total, be thought of in terms of the proportion of pore spaces in the dust-free coarse sample which are filled. An attempt to produce a range of mixtures from dust-free up to the ‘‘critical mixture’’, where all pore spaces are filled, guided initial choices of dust mass fractions. The critical mixture concept is in fact a less useful definition in practice since the coarse component, in all but the most dust-free mixtures, will be pushed apart by intervening dust particles. Additionally, the dust within the pores may undergo some degree of compaction due to the weight of the overlying material. This effect will be enhanced if coarser (and therefore denser) material is included, as in a mixture. Thus the value for the bulk density of the fines (needed to calculate the critical mixture) may cover a significant range, even within a single sample.

Smooth variation of measured diffusion coefficient is expected as the mass fraction of dust is increased from pure glass beads to pure dust. These experiments exhibit that diffusion through pure unpacked dust can be several  $\text{cm}^2 \text{s}^{-1}$  higher than the value found for glass beads, while for mechanically compacted dust it can be much lower. As stated above, the weight of the dense glass beads should act, at small dust fractions, to compress the dust toward a packed configuration. Mechanical compaction is not applied to these samples.

### 4.2.2 Salt crusts

Magnesium sulfate was chosen to study the behavior of salt crusts as barrier-forming phenomena due to its availability, crystallization to a well-known phase (epsomite:  $\text{MgSO}_4 \cdot 7\text{H}_2\text{O}$ ) under ambient conditions, and the known existence of sulfate salts on Mars (*Clark and van Hart, 1981; Vaniman*

*et al.*, 2004; *Yen et al.*, 2005).

Distilled water is saturated with 250 g of anhydrous  $\text{MgSO}_4$  per liter and then mixed with a given mass of 50–80  $\mu\text{m}$  glass beads and excess distilled water to produce a slurry of dissolved salt and beads. A mold consisting of a plastic ring and support wires (see Figure 4.1a), is attached to a plastic base with water-resistant grease. The walls and base of this mold are coated with a thin layer of WD-40 lubricant to facilitate removal of the dried crust. Once poured into the mold, the slurry and mold were agitated to remove any trapped air and produce a flat upper surface; any excess was scraped off. Slurries were allowed to evaporatively dry in ambient lab conditions for approximately 6 hours. Internal cohesiveness then allowed them to be removed from the flat mold base and placed on a coarse wire mesh in a forced draft, thereby continuing to dry from both surfaces of the crust. After approximately 24 hours, when the crusts were completely dry, they were placed in a desiccator and moved into the freezer to thermally equilibrate with the environment prior to the start of an experiment.

Slurries were prepared with 0.5, 1.0, 2.5, 5.0, 7.5, and 10.0 wt%  $\text{MgSO}_4$  (MW= 120.37 g mol<sup>-1</sup>). When allowed to crystallize at ambient conditions, epsomite is produced (MW=246.37 g mol<sup>-1</sup>) giving salt contents of 1.0, 2.0, 4.9, 9.7, 14.2, and 18.4% by weight epsomite.

To perform diffusion measurements, the 1 cm salt crusts are placed over an ice-filled 1 cm caddy and secured in place with water-resistant vacuum grease. Following an experiment, the ice surface is examined to determine if there were any leaks between the ice and salt caddies. The low-pressure, low-temperature environment gives rise to distinct ice surface morphologies if the vapor escapes in a rapid or asymmetric way. If any evidence for a leak is observed, the data and sample are discarded.

X-ray powder diffraction was performed on the sample crusts before and after exposure to experimental conditions. Most of the x-ray spectrum indicated the presence of an amorphous phase, *i.e.*, the glass beads. The peaks that did occur in the spectrum matched the intensity and location expected for epsomite. Samples of crust which incorporated greater proportions of material from the interior of the crust exhibited weaker peaks, indicating that the salt concentration decreased toward the caddy center. To examine the surface crusts more closely, the top and bottom surfaces of the crust were scraped following an experiment. The bottom surface of the crust (*i.e.*, the surface adjacent to the ice during the experiment) showed the same strong set of epsomite peaks as before exposure to experimental conditions. The upper surface scrapings (*i.e.*, from the surface exposed to the dry chamber atmosphere) exhibited a complete change of spectrum and revealed only the presence of hexahydrate, indicating a loss of the loosely bound seventh water molecule under desiccating low-pressure, low-temperature conditions. It is unknown how deeply into the sample this conversion penetrates.

For a 1-cm-thick crust of an initial composition of 14.2 wt% epsomite, the total amount of epsomite present is approximately 8.2 g. If it is assumed that one half of the crust converted

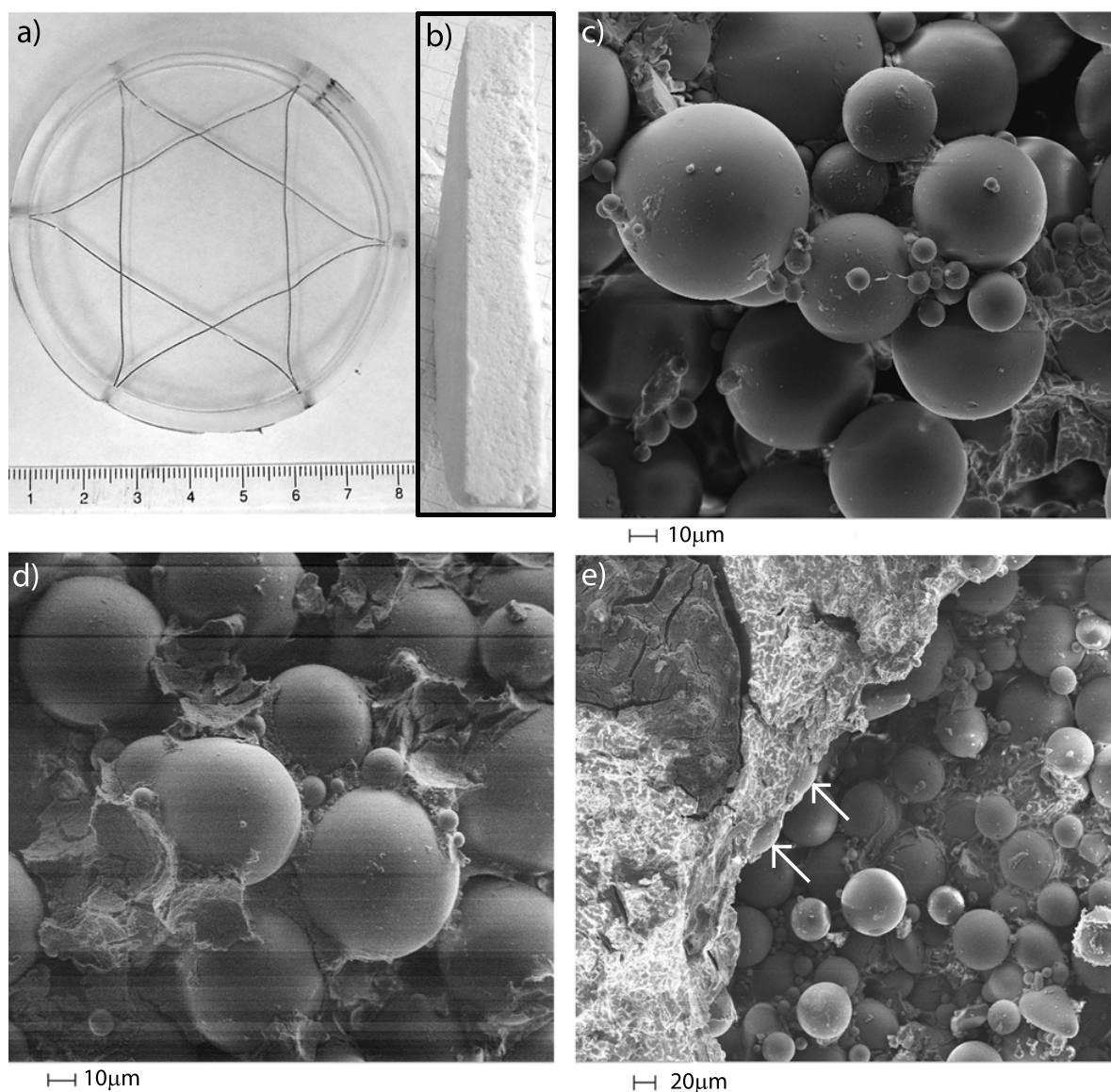


Figure 4.1: a) Empty salt crust caddy (1 cm depth) showing support wires. b) A cross section of a crust grown without wires. c)–e) SEM images of a 14.2 wt% epsomite salt crust after exposure to experimental conditions: c) Interior of crust: view of a cluster of beads held together by salt, beads much smaller than 50–80  $\mu\text{m}$  are present in a significant number and frequently fill pore spaces between larger beads. d) Interior of crust: section of crust showing salt features filling void spaces between larger grains. Dehydration to hexahydrate is the presumed cause of the fracturing. e) Surface of crust: the left side of the image is dominated by an efflorescent crust of hexahydrate which embeds some beads (arrows) but is predominantly pure salt.

completely to hexahydrate, the mass of water lost would be 0.3 g. This is less than 4% of the total amount of mass lost through ice sublimation and contributes a negligible error to the measured flux.

The reconstructive transformation which takes place between epsomite and hexahydrate results in the destruction of large crystals in favor of much smaller crystallites. This micro-fracturing could increase the available vapor transport volume. The timescale of this transformation under these experimental conditions is not constrained, but linear mass loss rates are observed after initial transients, suggesting a diffusion coefficient which is largely constant in time. This implies two possibilities. First, transformation may be rapid, occurring in the initial few hours of exposure to vacuum, and thus the diffusion coefficient measured is that of glass beads encrusted with fractured, dehydrated salts. The other possibility is that the transformation is gradual, occurring throughout the experimental duration, but has an effect on the diffusivity which is small compared to that arising from the overall salt content.

## 4.3 Analysis

### 4.3.1 Corrected diffusion coefficients

Unconsolidated samples rest directly on the ice while crusts have a discernible gap between the ice surface and the bottom of the sample. The vapor density difference across the sample is derived from measurements made at the ice surface and the position of the hygrometer. These may be different from the true lower and upper boundaries of the porous medium. By assuming that all fluxes are proportional to the density gradient across any given layer (whether free-gas or porous medium), and applying the conservation of mass requirement that all fluxes be equal in the absence of ice deposition or loss, a correction term is established which accounts for diffusion through the simulant-free portions of the column. The derivation of this correction is detailed in Section 3.4.2 and *Hudson et al.* (2007).

The necessary measurements of uncorrected diffusion coefficients at several sample thicknesses were done for 50–80  $\mu\text{m}$  glass beads in the 250 K environment. The correction term was found to be at most 0.06 cm, or a 6% correction for a 1 cm thick sample. The shift in calculated diffusion coefficient is much less than the experimental error, even for the thinnest samples. For this reason, uncorrected measurements for salt crusts, though conducted on samples  $\sim 1$  cm thick, are accurate within the systematic errors. Mixtures were tested with sample columns 5 cm thick, a thickness which has a minimal correction contribution even at the warmer temperatures of *Hudson et al.* (2007).

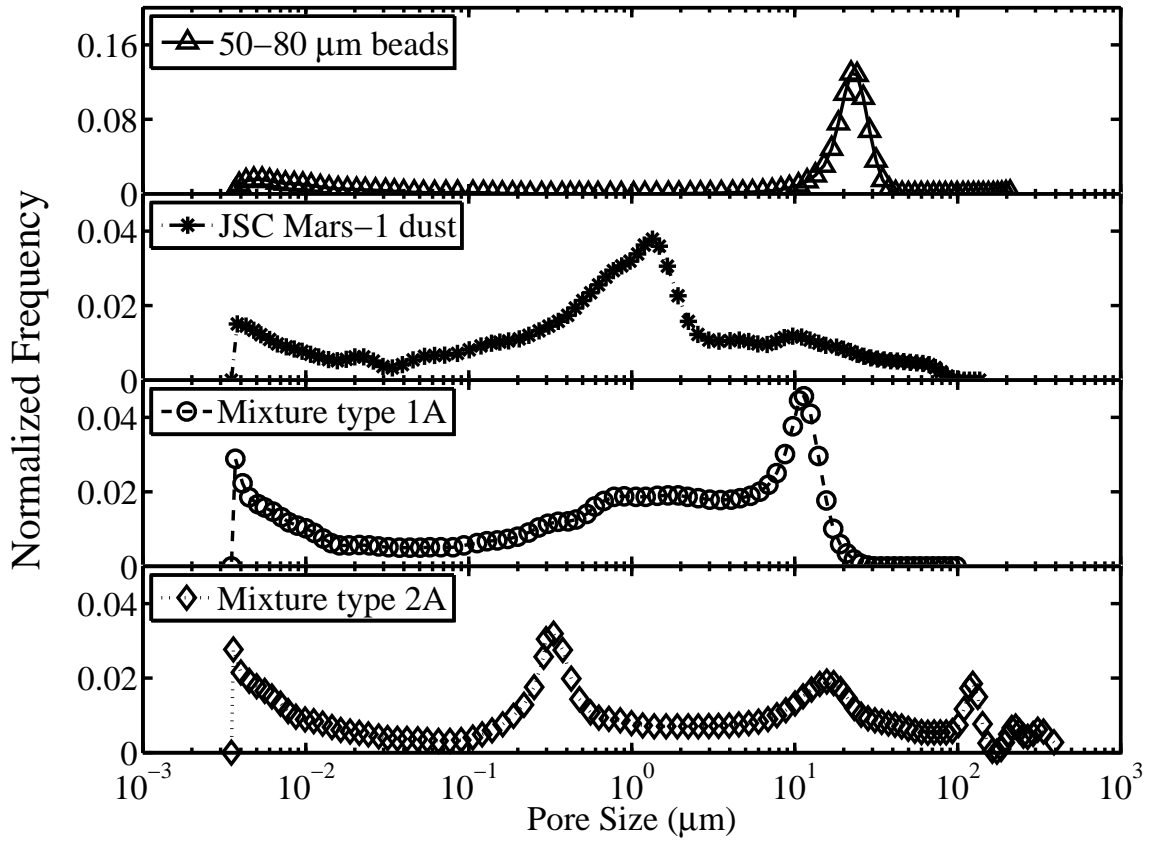


Figure 4.2: Normalized pore size distribution functions for four samples analyzed with mercury porosimetry

### 4.3.2 Pore structure

The porosity of the glass beads was determined with the basic method given in Section 3.3, while for mixtures it was estimated using equation (4.1). However, this latter method ignores the dust which may not only fill the interstices of the host sand but may also settle between the sand grains during agitation, thus pushing them apart and increasing the ‘unfilled’ volume. Salt crusts are even less amenable to simple interrogations or estimates of pore volume due to the unknown distribution of epsomite and sand grains following crystallization. Nevertheless, it is possible to determine the obstruction factor, the ratio of porosity to tortuosity, once the diffusion coefficient has been measured.

Four simulants were sent to Porous Materials, Inc. for analysis by mercury porosimetry. This technique reports pore size distributions, median pore diameter, pore volume and surface area. The simulants chosen for this analysis were pure 50–80  $\mu\text{m}$  glass beads, pure crushed JSC Mars-1 dust, and the two most dust-rich varieties of Mixture Type 1 and Mixture Type 2 (Varieties “A” in Table 4.1). The pore-size distributions for these four materials are plotted in Figure 4.2.

Figure 4.2 reveals that the pore size for the 50–80 micron glass beads peaks sharply at  $\sim 20$ –

25 microns. All distributions show significant tails at very small pore diameters, *i.e.*, 10 nanometers or less. These are likely to represent surface roughness, cracks, and other defects within individual grains in addition to very small passages between grains. While these passages do contribute marginally to the diffusible volume if interconnected, and to the tortuosity if blind, their contribution to the total flux will be negligible. As shown in *Clifford and Hillel* (1983), where pore sizes down to 1 nm are considered, pore distributions containing even a few percent porosity in larger (*i.e.*, micron-sized) pores experience most of their diffusive flux through these large spaces.

Examining the individual distributions reveals some interesting features. In crushed JSC Mars-1, the peak pore size, which is centered approximately on 1 micron, is much broader than for the more regular glass beads, and the pore distribution goes to zero almost nowhere below 100  $\mu\text{m}$ . In the mixture containing both glass beads and JSC Mars-1 dust, the modal peak falls between the modal peaks of the two mixture components at about 10 microns. The pore diameter distribution in this material drops sharply to the right of this peak, being zero above 30  $\mu\text{m}$ . This suggests that self-compaction and the availability of small grains acts to close off the largest pore spaces. Comparing the mixture of beads and JSC Mars-1 to the mixture composed of beads and 1–3  $\mu\text{m}$  dust further underscores the effects of self-compaction. The micron-sized dust is much less dense than the crushed JSC Mars-1 and does not compress as readily under its own weight. The resulting multi-modal distribution has pore spaces indicative of close-packing of dust grains (*i.e.*, the peak at 0.3  $\mu\text{m}$ ), but also possesses a very significant fraction of pores greater than 100 microns across. In a material containing such large pores, which might be termed a ‘fairy-castle’ structure, these open spaces will accommodate the majority of the diffusive flux. However, these large pore spaces are unlikely to be connected as a high-diffusivity conduit throughout a thick porous medium; transport will be governed by the average resistive path experienced by a diffusing molecule which shall include segments of less open material. It should be cautioned that mercury porosimetry is a high-pressure intrusive technique and may result in a rearrangement of pores and particles; very fragile structures may be disrupted.

Of these four simulants, the one with the distribution which appears to have the lowest amount of large cross-section pore space available for transport is the 40% mass-fraction fines mixture of glass beads and crushed JSC Mars-1 dust. Effects that may be responsible for closing off large pores include altered bulk density, which enhances self compaction, and the availability of small particles to fill in the interstices. For further analyses of a broader selection of particle sizes and shapes, the reader is referred to the recent work of *Sizemore and Mellon* (2007). In Section 4.4.5 porosimetry measurements are used to estimate the tortuosity for these four samples.

## 4.4 Results

This section details the results of these investigations into the diffusive properties of glass beads, salt crusts, two types of bead and dust mixtures, and two types of pure dusts under Mars-like conditions. Figure 3.10 shows the vapor fluxes as a function of temperature for all simulants along with the evaporation rate curve for bare ice as given by *Ingersoll* (1970) for a dry atmosphere (data from the experiments of Chapter 3 are also included in that figure). Slightly different background temperatures used during the experiments result in the offset indicated by the arrows. The shift is nearly horizontal, indicating that flux is relatively insensitive to these small changes in absolute temperature.

### 4.4.1 50–80 $\mu\text{m}$ glass beads at 250 K

Glass beads are the main component which comprises most of the more complex simulants used. Measurement of the compositionally and geometrically simple glass beads facilitates comparison with previous experiments (*Hudson et al.*, 2007). The beads are all nearly perfect spheres, 50–80  $\mu\text{m}$  in diameter. Within a factor of two in friction threshold velocity, these are similar to the 100  $\mu\text{m}$  size of the most easily lofted particles under martian conditions (*Greeley et al.*, 1980).

The dominant size of the beads is 50–80  $\mu\text{m}$ , but the distribution has a significant tail down to smaller sizes as revealed in the particle size analysis in Figure 3.5 b); the smaller spheres can be seen in the SEM images in Figure 4.1c and 4.1d. For close-packed particles with such a size distribution, the minimum pore size is on the order of 10  $\mu\text{m}$  and the maximum is  $\sim 80 \mu\text{m}$  (see Section 3.3.1). At 600 Pa, the mean free path is  $\sim 11.5 \mu\text{m}$  and diffusion should be dominated by Fickian processes of molecule-molecule collisions, but Knudsen interactions will contribute to an observable extent. The data for glass beads at 250 K in Chapter 3 are included in the data presented here. The weighted mean and standard deviations of the corrected diffusion coefficients is  $3.69 \pm 0.24 \text{ cm}^2 \text{ s}^{-1}$ . As mentioned in Section 4.3, the correction term for this simulant is  $z_{\text{corr}} \leq 0.6 \text{ mm}$ , and Figure 4.3 shows both the raw and corrected values. All raw values greater than 2 cm thicknesses fall within one standard deviation of the weighted mean.

If the Fickian dependence of diffusion coefficient on temperature and pressure,  $T^{3/2}$  and  $P^{-1}$ , respectively, is used and typical Mars temperatures and pressures of 200 K and 600 Pa, respectively, are chosen,  $D(200 \text{ K})$  is determined to be  $2.73 \pm 0.28 \text{ cm}^2 \text{ s}^{-1}$ . The glass beads measured in these experiments have a mean geometric porosity of  $44 \pm 2\%$ , as determined from volume and mass measurements of the bulk sample and knowledge of the true density of the particles.

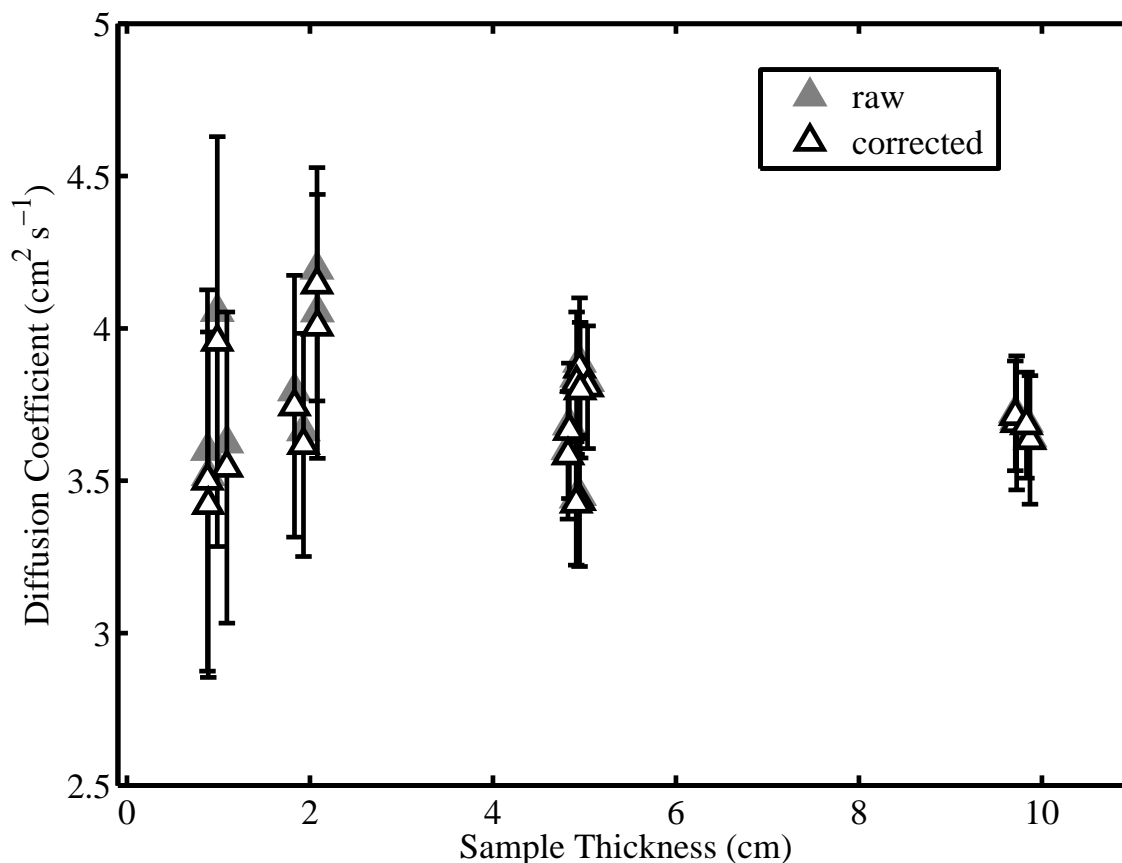


Figure 4.3: Raw and corrected diffusion coefficients for 50–80  $\mu\text{m}$  glass beads at 250 K and 586 Pa. The correction term is only 0.06 cm; raw values are nearly indistinguishable from corrected values.

#### 4.4.2 Epsomite salt crusts

The presence of sulfate salts on Mars, the frequency of observed duricrusts, and their potential for reducing soil porosity motivate their investigation. As convenient and consistent samples, glass beads cemented with magnesium sulfate salt are created in the laboratory and the diffusion coefficient is measured for a range of salt contents. Some inhomogeneities are observed within the salt crusts when they are broken following experiments. Outer layers of the crusts tend to be more cohesive than the center in samples with high salt contents. These layers may account for the majority of the diffusive resistance of the samples.

The diffusion coefficient data for the salt crusts is presented in Figure 4.4 which shows that the diffusion coefficient for crusts decreases with increasing salt content. The negative trend is expected, and a reduction in the diffusion coefficient by nearly a factor of 8 over that of pure glass beads occurs for salt concentrations of 18 wt% epsomite. Lacking measurements of the porosity, a tortuosity for the salt crusts cannot be calculated. Obstruction factors vary as the diffusion coefficient, and overall the factor is reduced from 0.14 to 0.02 between salt-free and the most salt-laden experiments.

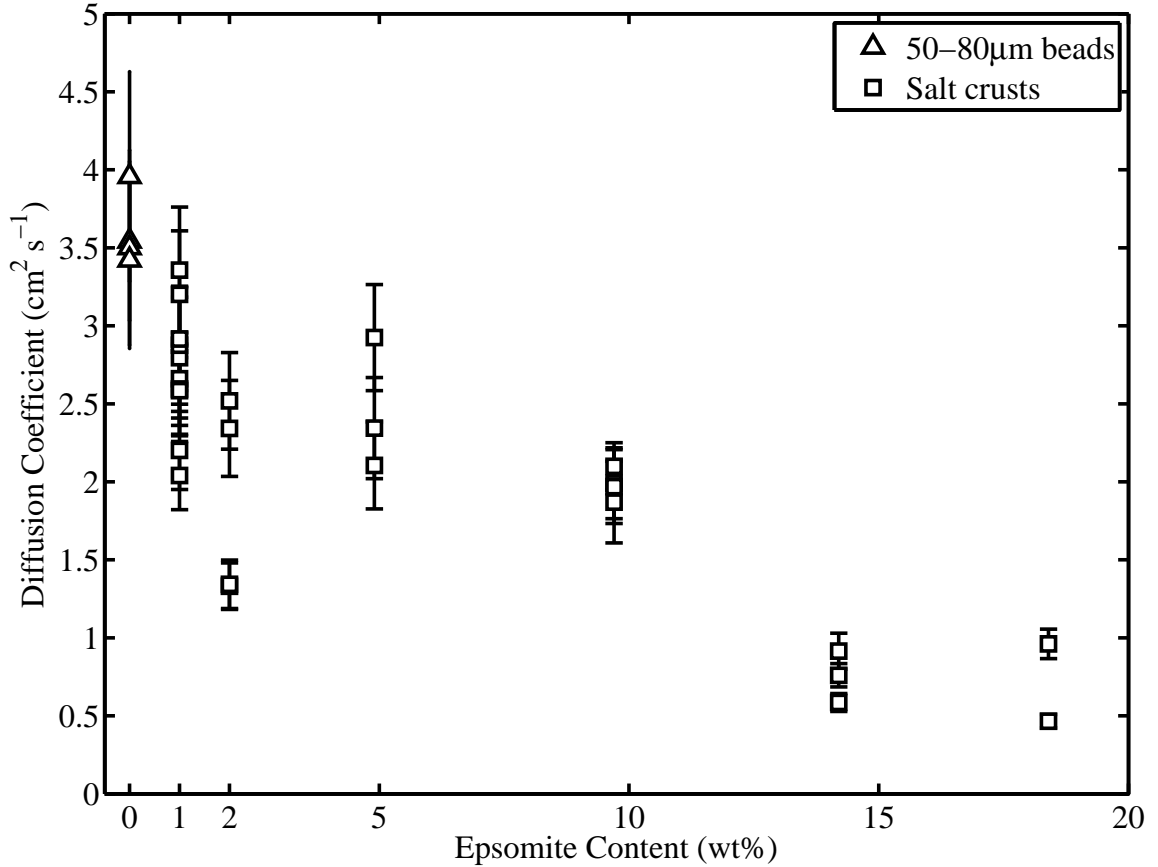


Figure 4.4: Diffusion coefficients for crusts of 50–80  $\mu\text{m}$  glass beads and  $\text{MgSO}_4 \cdot 7\text{H}_2\text{O}$  at 250 K and 586 Pa

#### 4.4.3 Mixtures

The inclusion of small particles within a matrix of larger clasts can reduce the porosity available for vapor transport and has the potential to significantly change the diffusion coefficient (*Farmer, 1976*). The diffusion coefficient for mixtures of glass beads with both crushed JSC Mars-1 and 1–3  $\mu\text{m}$  dust are plotted in Figure 4.5. For Mixture Type 1 (glass beads and crushed JSC Mars-1), the diffusion coefficient and obstruction factor decrease strongly with increasing dust mass fraction while measured porosity increases. However, for Mixture Type 2 (1–3  $\mu\text{m}$  dust and glass beads), neither diffusion coefficient nor obstruction factor trend strongly with dust mass fraction, but an obvious positive correlation with porosity remains.

The calculated porosity for both types of mixtures are displayed in Figure 4.6. Also included is data for the measured porosity of packed samples of both pure crushed JSC Mars-1 and pure 1–3  $\mu\text{m}$  dust. The trend for both types of mixtures as the mass fraction of dust increases is for the total porosity to increase and approach the values exhibited by pure dust. In the case of bead and 1–3  $\mu\text{m}$  dust mixtures, this value seems to be reached at  $X_f \approx 40\%$ , the trend with beads plus crushed JSC

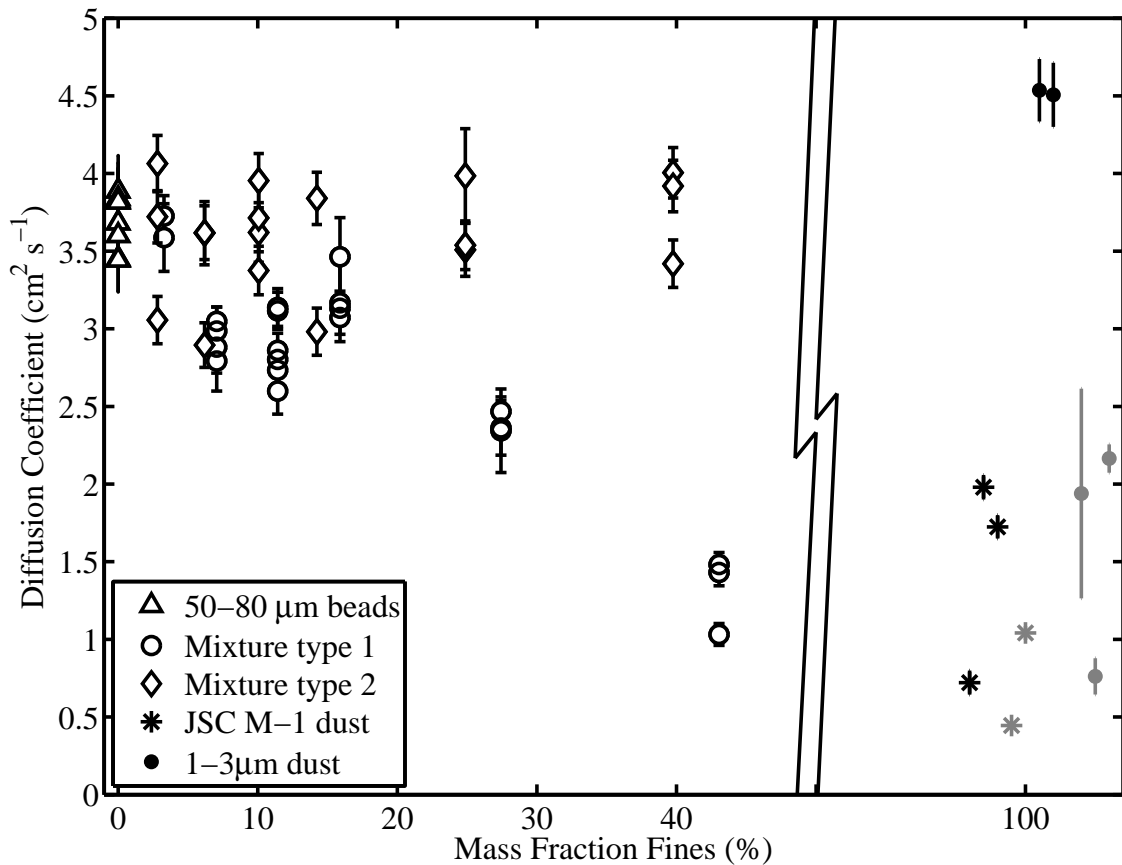


Figure 4.5: Diffusion coefficients for mixtures of 50–80  $\mu\text{m}$  glass beads with crushed JSC Mars-1 (Mixture Type 1, circles), mixtures of glass beads with 1–3  $\mu\text{m}$  dust (mixture type 2, diamonds), and diffusion coefficients for pure dusts (asterisks and filled circles). All data obtained at 250 K and 586 Pa. Mechanically compacted dust experiments are indicated in gray. All data to the right of the break are 100% dust by mass, but are separated for clarity.

Mars-1, if linear, would reach this point at approximately  $X_f \approx 60\%$ . The overall increase in porosity with dust content indicates that the included dust tends to coat the larger particles upon mixing and acts to keep them apart, thereby substantially increasing the total volume available. This is in contrast the case where dust might fill the available pore spaces of a coarse medium without increasing the spacing between larger particles.

The large increase in measured porosity for the micron-sized dust mixtures is counterbalanced by an apparent minor increase in the value of tortuosity, such that the obstruction factors ( $D/\mathcal{D}_{12}$ ) hardly change with  $X_f$ . For mixtures containing beads and crushed JSC Mars-1, however, the increase in porosity is apparently superseded by a tortuosity which increases faster, leading to smaller obstruction factor with larger dust mass fraction. Since tortuosity should be constant with diffusion regime, all else being equal, it must be the case that high proportions of micron-scale dust give rise to very small pores, changing the overall structure and producing a greater tortuosity.

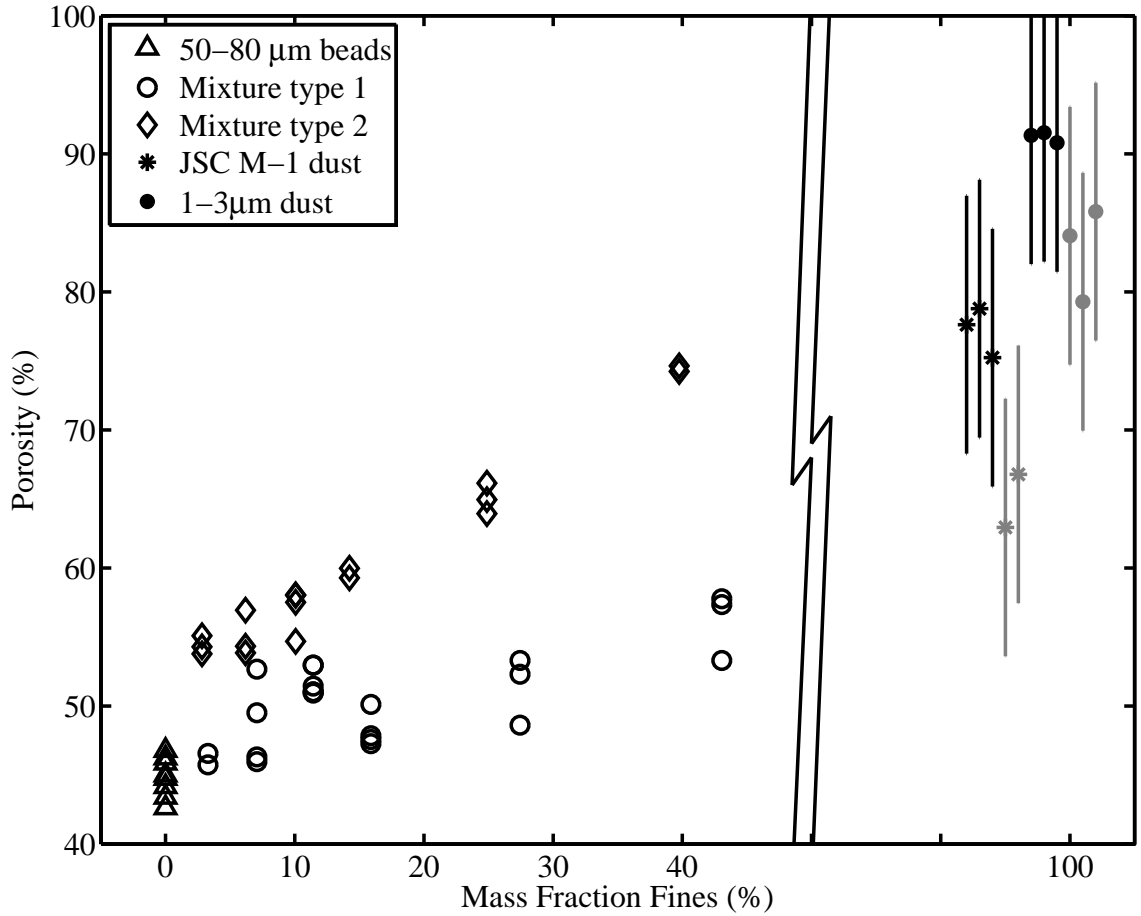


Figure 4.6: Porosities for pure glass beads (triangles), mixtures of beads and fine dusts (open circles and diamonds), and pure fine dusts (asterisks and closed circles). Mechanically packed dust samples are in gray. All data to the right of the break are 100% dust by mass, but are separated for clarity. Porosity of the mixtures of glass beads and crushed JSC Mars-1 (Mixture Type 1) increase slowly, while the less self-compacting mixtures containing beads and micron-sized dust achieve much higher porosities.

#### 4.4.4 Dusts

Pure samples of the 1–3  $\mu\text{m}$  dust and crushed JSC Mars-1 were examined in both packed and unpacked configurations. Loose dust may be considered a crude approximation to airfall dust, while compaction simulates the effect of burial.

Loose dust was poured into the sample caddy and planed off to 5 cm thickness. The low-density 1–3  $\mu\text{m}$  dust exhibited no observable self-compaction even in samples of this thickness. Both dust types were seen to deposit with visible sub-millimeter gaps between aggregates. Though aggregates of the size and density observed in this sample handling method are unlikely to be supportable by the thin martian atmosphere, airfall dust deposits on Mars will likely form low-density aggregates in response to electrostatic forces, resulting in deposits of even lower bulk density.

For compacted samples, the equivalent of between 5 and 8 cm of loose dust was pressed into the sample caddies with a flat circular plate. Air in the pore spaces was allowed to escape around the edges of the plate. Following compaction, the sample was weighed to determine a bulk density and total thickness.

The experiments show that packed and unpacked JSC Mars-1 has a range in diffusion coefficient from 0.45–1.98 cm<sup>2</sup> s<sup>-1</sup>, with a weighted mean value of  $0.77 \pm 0.04$  cm<sup>2</sup> s<sup>-1</sup>. Data from both packed and unpacked samples are included in these values since their ranges overlap. The 1–3 μm dust exhibits a larger distinction between loose and compacted samples, with weighted mean values of  $4.71 \pm 0.22$  and  $1.64 \pm 0.11$  cm<sup>2</sup> s<sup>-1</sup>, respectively.

#### 4.4.5 Sample tortuosity

In Section 3.5.1.3 independent Fickian and Knudsen diffusion coefficients were determined and a tortuosity was calculated for 50–80 μm glass beads of  $1.8 \pm 0.6$ . This compares favorably with earlier measurements of tortuosity of glass spheres such as those by *Hoogschagen* (1955) who determined  $\tau=1.3$ –1.5 and *Currie* (1960) who theoretically calculated values between 1.3 and 1.7 and experimentally found  $\tau=1.4$ –2 for larger spheres (380 μm to 6 mm).

Here the method of *Zalc et al.* (2004), described in Section 2.5, is employed to estimate  $D_K$  and then the geometric (*i.e.*, independent of diffusion regime) tortuosity for the four selected samples of Section 4.3.2. This calculation takes as inputs the measured effective diffusion coefficient, porosity, free-gas diffusion coefficient, and the chord length distribution function,  $p(l)$ .

To retain consistency with earlier work (*Hudson et al.*, 2007) and with the work of a number of previous investigators, the method of *Wallace and Sagan* (1979) is used to determine the free-gas diffusion coefficient,  $\mathcal{D}_{12}$ , noting that other calculation methods produce values that are different from this by as much as a factor of 2, but are typically closer.

The chord length distribution is calculated from the pore size distribution,  $V(x)$ , (Section 4.3.2 and Figure 4.2 using the method described in *Gille et al.* (2002), which approximates the pore spaces as cylinders of varying lengths. Thus,  $p(l)$  is given by

$$p(l) = \frac{\int_0^L x \cdot A_0(l, x) \cdot V(x) dx}{\int_0^L x \cdot V(x) dx}, \quad (4.2)$$

where  $l$  is random chord length within a pore,  $x$  is the pore diameter,  $L$  is a length parameter, and  $A_0(l, x)$  is the chord length distribution of an infinitely long cylinder of diameter  $x$ .  $A_0(l, x)$  is given

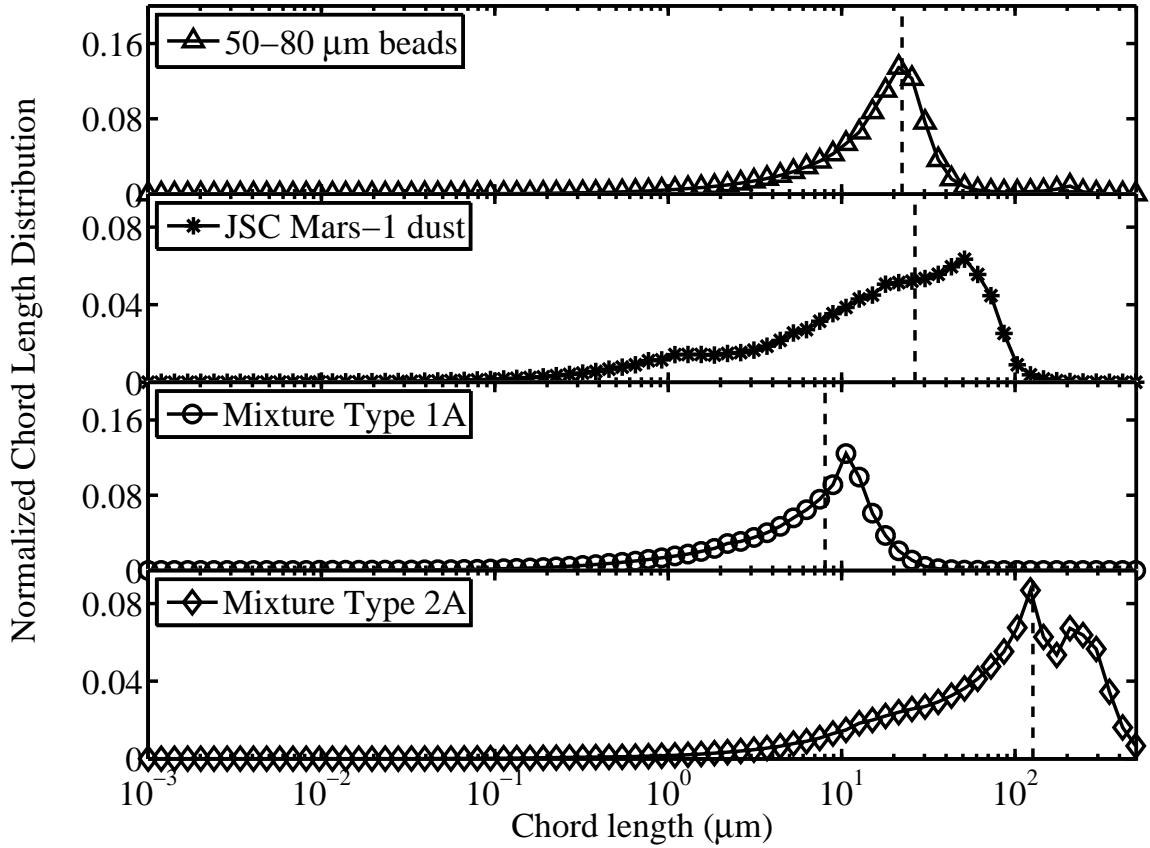


Figure 4.7: Normalized chord length distributions functions computed from pore size distributions. Vertical dashed lines are first moments of the chord length distributions,  $\langle l_p \rangle$ .

by *Gille et al.* (2001) as expressions involving Gauss' hypergeometric functions,  ${}_2F_1$ :

$$A(l, x) = \frac{3l}{4x^2} \cdot {}_2F_1\left(\frac{1}{2}; \frac{5}{2}; 3; \frac{l^2}{x^2}\right), \quad l < x \quad (4.3)$$

$$= \frac{3x^3}{4l^4} \cdot {}_2F_1\left(\frac{1}{2}; \frac{5}{2}; 3; \frac{x^2}{l^2}\right), \quad l > x. \quad (4.4)$$

The assumption of cylindrical pores may be violated in media with irregularly shaped grains.

The first and second moments,  $\langle l_p \rangle$  and  $\langle l_p^2 \rangle$ , are computed in the standard way. Applying these techniques, chord length distributions and first moments are obtained, and these are displayed in Figure 4.7. Table 4.2 displays the mean diameter,  $\bar{d}$ , and first moment of the chord distribution,  $\langle l_p \rangle$ . Also computed and tabulated are the quotient  $\langle l_p^2 \rangle / 2\langle l_p \rangle^2$ , which describes the deviation of the chord length distribution function from an exponential distribution, and the calculated tortuosity,  $\tau$ .

As Table 4.2 illustrates, the value of  $\tau$  thus determined for glass beads is close to the expected values of  $\sim 1.5$ . The other tortuosity values cover a range up to 6, which is high compared to

ranges used in early estimates of tortuosity (*e.g.*, 3–5 in *Smoluchowski (1968)*), and to more recent experimental studies (*Sizemore and Mellon, 2007*). Uncertainty in these numbers arises both from the variation in  $\mathcal{D}_{12}$  and the possible violation of the cylindrical pore assumption. Taken together, these tortuosity estimates are not appreciably different from those used in previous diffusion studies, but their variation underscores the uncertainty of this quantity for many porous materials and highlights the importance of measuring the effective diffusivity directly, in the Fickian regime if possible. It would be useful to further explore the effects of particle size mixtures and salt content on pore structure and pore size distribution, and to determine the conditions which give rise to the greatest change in soil diffusive properties.

#### 4.4.6 Summary

Table 4.3 presents a summary of the data for each type of simulant. For mixtures and salt crusts, the range of observed values of  $D$ ,  $\phi$ , and  $D/D_{12}$  are presented. Other simulants show weighted means and standard deviations.

Correction terms are applied to experiments performed on glass beads at 250 K under  $\text{CO}_2$ , though this correction ( $z_{\text{corr}} = 0.6$  mm) results in a comparable but smaller shift in the data than systematic scatter and formal errors. Corrections for salt crusts are determined to be unnecessary because the correction term for pure glass beads of the same thickness was found to be negligible at these temperatures. All other experiments are performed with 5 cm thick samples, which provides enough diffusive resistance to reduce the correction term below systematic errors; hence the values reported are unmodified.

Diffusivities for all simulants fall within the range of 0.47–4.7  $\text{cm}^2 \text{s}^{-1}$ , as seen in Figure 4.8. Extrapolation to the Mars-appropriate conditions of 200 K and 600 Pa via the Fickian dependence of the diffusion coefficient on temperature and pressure yields the range 0.34–3.30  $\text{cm}^2 \text{s}^{-1}$ . The obstruction factor for most simulants is between 0.02 and 0.20. Tortuosities calculated for four simulants cover a range of 1.5–6.

Simulant	$\phi$ , %	$\bar{d}$ , $\mu\text{m}$	$\langle l_p \rangle$ , $\mu\text{m}$	$\langle l_p^2 \rangle / 2 \langle l_p \rangle^2$	$\tau$
50–80 $\mu\text{m}$ Beads	44	18.74	22.29	1.501	1.66
Crushed JSC Mars-1	77	5.35	26.46	1.002	6.01
Mixture Type 1A	56	4.42	8.03	0.794	1.68
Mixture Type 2A	75	32.7	126.65	0.903	3.82

Table 4.2: Porosities, average pore diameters, first moments of the chord length distributions  $\langle l_p \rangle$ , the exponential distribution deviation term, and tortuosities for four samples analyzed with mercury porosimetry.

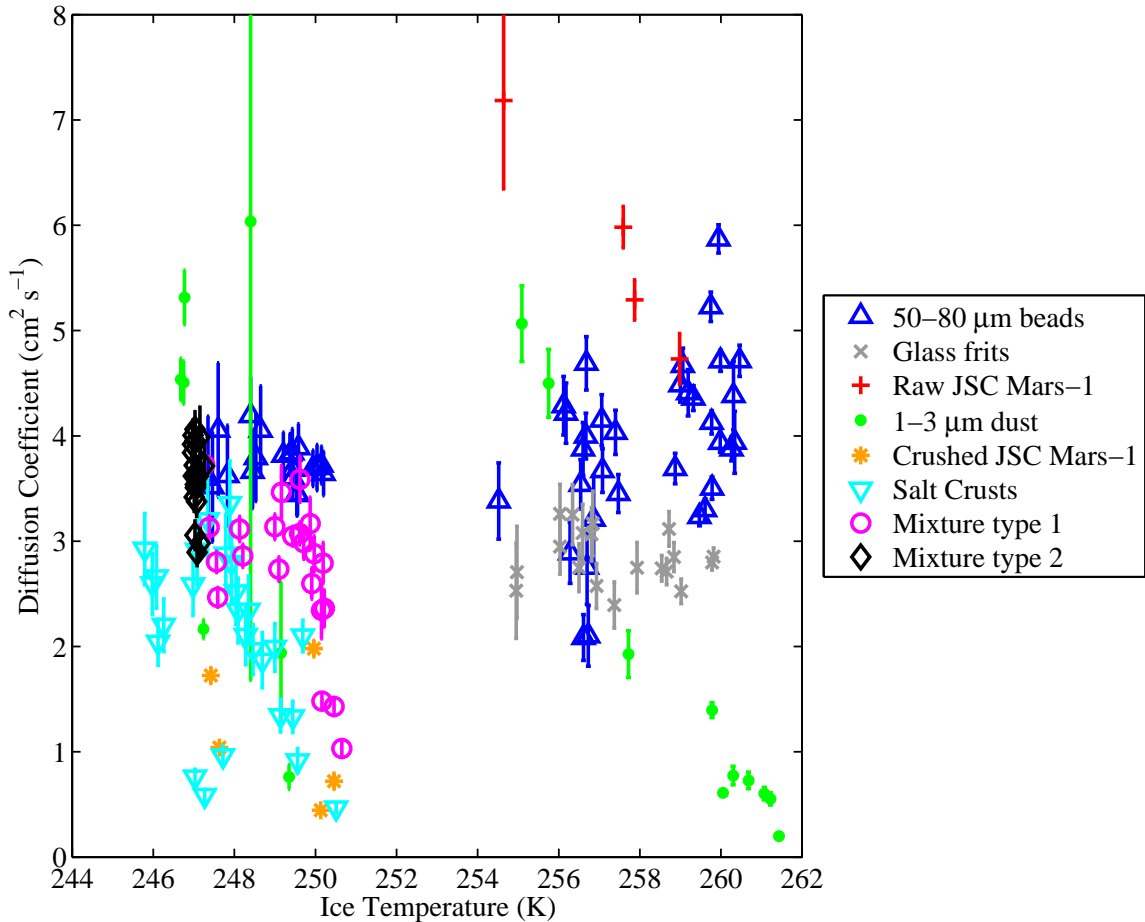


Figure 4.8: Diffusion coefficients for all simulants from Chapter 4 and Chapter 3.

Sample	$T_{\text{ice}}$ , K	$D$ , $\text{cm}^2 \text{s}^{-1}$	$D^1$ , $\text{cm}^2 \text{s}^{-1}$	$\phi$ , %	$\mathcal{D}_{12}$ , $\text{cm}^2 \text{s}^{-1}$	$D/\mathcal{D}_{12}$
50–80 $\mu\text{m}$ beads	$249.0 \pm 0.4$	$3.69 \pm 0.24$	$2.57 \pm 0.16$	$44 \pm 2$	$24.5 \pm 3.0$	$0.150 \pm 0.014$
Beads + $\text{MgSO}_4 \cdot 7\text{H}_2\text{O}$	$247.9 \pm 0.4$	$0.47 - 3.36$	$0.34 - 2.34$	N/A	$24.8 \pm 1.5$	$0.019 - 0.133$
Beads + JSC Mars-1	$249.4 \pm 0.4$	$1.03 - 3.73$	$0.74 - 2.68$	$46 - 58$	$25.0 \pm 1.6$	$0.041 - 0.150$
Beads + 1–3 $\mu\text{m}$ dust	$247.1 \pm 0.2$	$2.90 - 4.06$	$2.11 - 2.90$	$54 - 66$	$24.8 \pm 1.5$	$0.117 - 0.160$
JSC Mars-1, loose	$246.7 \pm 0.2$	$1.47 \pm 0.08$	$1.03 \pm 0.06$	$77 \pm 9$	$24.7 \pm 1.5$	$0.060 \pm 0.006$
JSC Mars-1, packed	$247.5 \pm 0.2$	$0.59 \pm 0.03$	$0.42 \pm 0.02$	$65 \pm 9$	$25.9 \pm 1.6$	$0.023 \pm 0.002$
1–3 $\mu\text{m}$ dust, loose	$248.9 \pm 0.2$	$4.71 \pm 0.22$	$3.36 \pm 0.16$	$83 \pm 9$	$24.9 \pm 1.5$	$0.190 \pm 0.015$
1–3 $\mu\text{m}$ dust, packed	$248.6 \pm 0.2$	$1.64 \pm 0.11$	$1.16 \pm 0.08$	$91 \pm 9$	$25.1 \pm 1.5$	$0.062 \pm 0.006$

Table 4.3: Summary of results for experiments carried out at 250 K and  $\sim 586$  Pa in  $\text{CO}_2$ . Weighted averages and standard deviations are given when samples are approximately uniform. Minimum to maximum intervals are given where variation among samples is responsible for the range of observations. [1] Diffusion coefficients extrapolated to 200 K and 600 Pa using  $D \propto T^{3/2}P^{-1}$ , as appropriate for Fickian diffusion

## 4.5 Discussion

### 4.5.1 Experimental errors

See Section 3.5.1.1 for a discussion of systematic errors in the experimental setup. In brief, variations exist because gas mixing in the chamber atmosphere which is not necessarily the same among

different experiments, and because the localized measurement of humidity may not reflect the average environment across the sample surface. These issues are mitigated by multiple experiments which improve measurement statistics.

In Section 2.6.2 (*Hudson et al.*, 2007), it was shown that thermodiffusion is less than concentration diffusion by a factor of  $0.8(m_2/m_1)(\Delta T/T)(p_1/\Delta p_1)$ . The largest value of  $\Delta T/T$  for any experiment is 0.015, while the average value is 0.009. For  $(p_1/\Delta p_1)$ , the extreme and average values are 1.8 and 1.2. Thus, the maximum expected contribution from thermodiffusion is 5% while more typical values are closer to 2%. In Section 2.6.3, an expression for the ratio of barodiffusion to concentration diffusion was given as  $0.6(\Delta p_0/p_0)$ . The maximum possible  $\Delta p_0$  is the saturation vapor pressure of water at 250 K (76 Pa), thus giving a maximum barodiffusion contribution of 7%. The value will be smaller for samples with higher permeability which therefore have smaller pressure gradients.

### 4.5.2 Advection

The corrected diffusion coefficient found for the glass beads in the experiments performed at 250 K is  $3.69 \pm 0.24 \text{ cm}^2 \text{ s}^{-1}$ . By comparison, the value obtained in Section 3.5.2 for these same simulants at 263 K is  $4.49 \pm 0.69 \text{ cm}^2 \text{ s}^{-1}$ . Adjusted for the 12 K temperature difference using a  $T^{3/2}$  dependence, and a  $P^{-1}$  correction for the overall 20 Pa pressure difference, this latter value would be  $4.13 \pm 0.64 \text{ cm}^2 \text{ s}^{-1}$  at 250 K. The lower vapor pressures should result in a lower advective contribution in the colder chamber. Reducing the 263 K experiment value by a further 3% (as calculated in Section 2.6.1) gives  $4.00 \pm 0.62 \text{ cm}^2 \text{ s}^{-1}$ , a value whose center is much closer to that measured in the 250 K chamber. However, since the error ranges of the two diffusion coefficients overlap, concluding that advection is responsible for the difference is not possible using this data.

### 4.5.3 Salts and salt crusts on Mars

The existence of salts on the surface of Mars is well established (*Clark and van Hart*, 1981; *Vaniman et al.*, 2004; *Yen et al.*, 2005), as is their association with surface crusts (*Landis et al.*, 2004; *Wang et al.*, 2006). *Chevrier and Mathé* (2007, and references therein) use lines of evidence from *in situ* and remote sensing observations to conclude that high sulfur abundances (compared to the surface of the Earth) are found over most of the known martian surface and that sulfur, particularly in the form of sulfate, is an important component in the evolution of the martian regolith.

The mobility of these salts and their observed ability to cement soil grains implies a potential for pore restriction or closure, and a concomitant reduction in the diffusivity of the salt-bearing soils and crusts. Recent observations by the Mars Exploration Rovers indicates the possibility of two populations of salt-bearing soils: lightly-cemented surface duricrusts containing a few percent of salt, and more loosely consolidated subsurface deposits of light-toned material which may be as

much as 50 wt% sulfate salt (*Cabrol et al.*, 2006; *Yen et al.*, 2007; *Wang et al.*, 2007).

Up to 50 wt% iron sulfate is inferred at the Paso Robles site observed by Spirit (*Cabrol et al.*, 2006). Many other sites present indications that magnesium sulfate is the dominant phase. Greater than 20 wt% in the wall of the trench named The Boroughs in Gusev crater was determined to be Mg and Ca bearing sulfate. The Mg/Ca ratio is high; approximately 5.

Analyses of sulfate stability fields under Mars surface conditions suggest that the most likely hydrated forms of magnesium sulfate are the monohydrate kieserite, or amorphous phases with from 1.2 to 2 molar units of water. Metastability may permit the persistence of more hydrated phases (*e.g.*, starkeyite,  $\text{MgSO}_4 \cdot 4\text{H}_2\text{O}$ ) which may have originally formed under more favorable climate conditions. The existence of sulfate phases common on Earth (6-hydrate hexahydrate or 7-hydrate epsomite) in the shallow subsurface of Mars is unlikely at present (*Vaniman et al.*, 2004).

Regardless of their hydration state, salt crystals may form barriers to diffusion in Mars soils just as they do on Earth. Caliche, a calcium-bearing mineral cement, frequently occurs in terrestrial desert environments, forming layers are often sufficiently resistive that they completely impede the movement of water resulting in perched water tables or aquacludes, the disruption of which produces artesian springs. Such phenomena have been hypothesized to occur on Mars as part of gully formation mechanisms (*Malin and Edgett*, 2000). Though magnesium-bearing salts are rather water soluble (56.0g/100g water for  $\text{MgCl}_2$ , 35.7g/100g for  $\text{MgSO}_4$  (*Lide*, 2003)) and would not form effective barriers to liquid water, they could impede or prevent the movement of vapor molecules.

In contrast to the sulfate-rich subsurface deposits observed by the rovers in isolated localities, indurated surface soils, called duricrust, have been observed at all Mars landing sites and are believed to be extensive (*Presley and Christensen*, 1989). The physical properties of surface crusts at the Viking lander sites have been calculated and similar properties over much of Mars' surface are predicted (*Moore*, 1992). The cohesive strength of surface soils at Viking sites falls in the range of 1 to 11 kPa (the cohesion of dry clayey silts on Earth, such as dried mud flats, is between 10 and 30 kPa). Crusts at the edge of trenches carved by the Opportunity rover are shown in *Weitz et al.* (2006), and the cementation of soils at Gusev is discussed by *Cabrol et al.* (2006) and *Landis et al.* (2004). Conclusive observations of the exact mineral composition and physical structure of these crusts does not yet exist, but evidence supports that the cohesion of Viking crusts is related to the presence of  $\text{SO}_3$  and Cl compounds (*Clark et al.*, 1977). Measurements by the MER instruments reveal large quantities of sulfates at numerous sites. Taken together, these data strongly suggest that salts, particularly sulfate salts, play a large role in duricrust formation. The laboratory-grown crusts have at most 10% by weight  $\text{MgSO}_4$ , a fraction smaller than that of the subsurface salts exemplified by the Paso Robles and Tyrone type soils.

In these experiments, a small amount of sulfate salt ( $\sim 1\%$ ) produces a small reduction in the measured diffusion coefficient of 50–80  $\mu\text{m}$  beads on the order of  $1 \text{ cm}^2 \text{ s}^{-1}$ . Further increases in

salt content have little apparent effect until >10 wt% epsomite, where reductions of  $D$  by a factor of 5 to 10 are observed.

As the water in the saturated slurry of the laboratory-grown crusts evaporates during formation, crystals preferentially form at points of low surface energy where nucleation is facilitated, such as grain contact points (see Figure 4.1 c). These crystals cement the grains of the material together once the water has evaporated, resulting in some reduction in porosity. Increasing the salt content may further reduce the porosity, but the majority of vapor transport pathways remain open. Beyond 5 wt% epsomite, the experimental scatter is reduced, which suggests that the overall change in pore geometry has become uniform among samples. As still more salt is added, the final porosity is substantially decreased, tortuosity rises, and  $D$  drops significantly. Laboratory salt crusts which completely block vapor diffusion have not been observed.

The protocol used for making laboratory crusts involves significant liquid water. This is not representative of any known present-day surface condition on Mars, yet geomorphic and geologic evidence, for example at Meridiani Planum, indicate that standing or subsurface water may have been a significant part of the geologic history in certain regions. The measurements here pertain to several studies invoking crust formation and solute transport processes that require small amounts of water. *Cabrol et al.* (2006) and *Landis et al.* (2004) discuss possible processes for the formation of salt crusts in the soils of Gusev crater. They suggest that humidity precipitated as frost during the cold Martian night, low thermal inertia of surface materials, and the presence of melting-point-lowering salts will result in a small transient liquid phase immediately following sunrise. Prior to evaporation, this liquid will dissolve salts which are then reprecipitated around the soil grains, resulting in crust formation. Such processes, they suggest, may only occur during particular seasons and possibly only during favorable years. *Wang et al.* (2006) conclude that the total amount of water activity necessary for the formation of Gusev crusts is likely to be low, as suggested by the limited quantity of evaporite deposition at the surface, the limited leaching of minerals by water, and the concentration of soluble elements. It may therefore be the case that the subsurface salt deposits and surface crusts are formed at different times, on different time scales, and with significantly different amounts of aqueous activity. The subsurface salts may be the source for a slow upward migration of chemical species which ultimately form the weak surface crusts. Taken together, the results of *Cabrol et al.* (2006); *Landis et al.* (2004); *Wang et al.* (2006) indicate formation mechanisms for salt crusts on Mars exist. Note, however, that they involve less water than the lab methods used here.

Intriguingly, the bright deposits revealed in rover wheel tracks have not yet been seen to outcrop anywhere in undisturbed regolith, leading to the hypothesis that their placement and vertical extent may be controlled by the surface-atmosphere interface through evaporation, set by the thermal wave penetration. The diffusion of oxidizing species from the atmosphere or surface layer of the regolith may also affect sulfate deposition. *Wang et al.* (2007) report long-term observations of two types

of light-toned soils (termed “yellowish” and “whiteish”) at the Tyrone site during the Spirit winter campaign. The “yellowish” soils are observed to change spectral character after at least 175 sols exposure to martian surface conditions, becoming more like the “whiteish” soils. This indicates that the more deeply buried “yellowish” soils were not in equilibrium with the current environment and are undergoing some sort of chemical change, which *Wang et al.* suggest may be dehydration of  $\text{Fe}_2(\text{SO}_4)_3 \cdot 7\text{H}_2\text{O}$ .

These experimental results suggest that surface duricrusts which show weak degrees of cementation and likely have  $< 10\%$  of soluble salt content will not present a substantial barrier to vapor transport, perhaps at most a factor of 2 reduction over uncemented soil. Higher salt content could lead to greater reductions in the diffusion coefficient, and soil salt contents of the appropriate concentrations have been observed. However, the deep sulfate salts which have thus far been uncovered by MER have appeared as loose subsurface powders with small particle sizes. If conditions elsewhere on Mars have permitted these subsurface salts to become mobilized and cemented, it is possible that the highest barriers to diffusion may be found beneath, rather than at, the surface.

#### 4.5.4 Diffusion in Mars dusts

Dust is present everywhere on Mars and is a significant part of the present-day climate cycle. It forms an active surface layer which may be lofted and re-deposited by dust storms, and may also be incorporated deep into the regolith. Two types of dust with differing particle size distributions are examined in both mechanically packed and unpacked configurations.

The diffusivity values for packed and unpacked JSC Mars-1 dust samples overlap and cover a range from 0.4–2.0  $\text{cm}^2 \text{s}^{-1}$ , indicating that mechanical packing does little to alter the properties of this simulant, and that there is wide variation between successive simulants. The large particle size range for this dust allows larger grains to interlock and create a supporting matrix which retains large pore spaces even under externally applied compaction. Still, each sample is unique in its precise geometry, and variations among samples exist. The larger spread in diffusion coefficients at  $X_f = 1$  than at lesser dust fractions (see below) indicates that the presence of larger particles at moderate dust fractions helps create a similar geometry from sample to sample through self-compaction, while the less massive pure dust samples are subject to greater variation. Mechanical packing has a significant effect on 1–3  $\mu\text{m}$  dust, decreasing its diffusivity from  $4.71 \pm 0.22$  to  $1.64 \pm 0.11 \text{ cm}^2 \text{ s}^{-1}$ .

Thin surface airfall dust layers would not be subject to compaction forces but might instead be “fluffed” by electrostatic forces. Burial depths of greater than several decimeters could create increased packing of interstitial airfall dust over a wide areal extent. To affect near-surface vapor fluxes, soils compressed by deep burial would have to be subsequently exhumed. Widespread exhumation is possible, but the thermophysical and spectral properties of such deposits would be distinct from loose dust. Dispersal in water could also produce low-porosity, low-diffusivity deposits

composed of fine dust or coarse/fine mixtures, but the invocation of liquid water as a component in the diagenesis demands additional support from available geologic or geomorphic context data.

The possibility that diffusion coefficients in dust-bearing soils could be reduced by a factor of 2 or more as a function of depth may significantly affect models which include interaction with more than the surface regolith.

#### 4.5.5 Sand and dust mixtures

Aeolian processes on Mars can produce well-sorted bedforms such as ripples (*Sullivan et al.*, 2005), and large-scale features such as dunes (*Greeley et al.*, 1992). The Microscopic Imagers on the MER spacecraft have observed soil grains down the limit of resolution (31  $\mu\text{m}$  per pixel), and an observable particle size range of 50–200  $\mu\text{m}$  has been determined (*Herkenhoff et al.*, 2004; *Jerolmack et al.*, 2006). Dust particles below the resolution limit are undoubtedly present at the rover sites and are likely to be present in significant quantities at dustier surface locales. The ubiquitous presence of dust on Mars' surface and observations of dust-rich, low thermal inertia regions suggest the strong possibility that mixtures of sand and dust-sized particles occur in some regions. Fluvial processes, volcanic processes, and impacts can agitate and mix surface regolith. If settling times after such disturbances are rapid, the unsorted or poorly-sorted character of the bulk material may be retained in the subsequent deposit. Agitation by shifting winds or long-term evolution through thermal expansion and contraction may mix initially separate particle size fractions at the surface in the absence of these more energetic processes.

Mixtures of two types have been produced and observed, using the 50–80  $\mu\text{m}$  glass beads as the coarse fraction and two types of dust particles. These are not meant to be representative of any particular Mars soil, but instead show the behavior of regolith diffusivity as a function of dust content. These experiments support the expectation that even in the absence of mobilized and recrystallized salt acting as a pore-filling agent, the diffusive properties of loose surface soils are affected by the presence of pore-filling materials such as dust. Martian fines have a mean particle size of a few microns (*Greeley et al.* 2000, and references therein), similar to the 1–3  $\mu\text{m}$  dust. Crushed JSC Mars-1 contains a range of particle sizes from sub-micron to 0.1 mm. These investigations have focused on homogeneous mixtures of sand and dust-sized particles, though *Farmer* (1976) suggests that thin dust mantles produced by airfall may fill the interstices of coarser material such that the diffusion coefficient is significantly reduced. The sample preparation method used includes initial mechanical agitation, but no subsequent compaction. The range of dust contents in the samples examined range from a clast-supported sediment with a very minor amount of included dust to a matrix-supported dust-rich deposit containing a minor proportion of separated, larger grains.

The difference in behavior between the two types of mixtures could be very significant for predictions of diffusive behavior of soils and sublimation lags on Mars. The trend seen in Figure 4.5

indicates that very small particles (1–3  $\mu\text{m}$  dust) admixed with coarser grains do little to increase the diffusive resistance to vapor flux if the whole sample is not mechanically compacted. The diffusion coefficient is independent of the mixing fraction up to  $X_f \approx 0.4$ .

If the distribution of finer material includes a broad spectrum of particle sizes, *i.e.*, grains roughly equivalent in size to the coarser fraction in addition to fine particulates (as in crushed JSC Mars-1), then there is a marked reduction in diffusivity as the mass fraction of fines increases. This effect, for uncompact mixtures, is a reduction in  $D$  to  $\sim 2.5 \pm 0.3 \text{ cm}^2 \text{ s}^{-1}$  at  $X_f = 0.4$ .

The measured geometric porosity for both types of mixtures increases with  $X_f$  in a linear fashion as shown in Figure 4.6. The porosity of micron-sized dust and beads would reach a value equivalent to pure-dust samples at around  $X_f = 0.6$ . The trend with JSC Mars-1 mixtures is shallower, but the ultimate porosity for pure dust is also lower. As seen in Table 3.1, the porosity of dusty soils can be quite large in the absence of mechanical compaction. Even when compressed, the minimum porosity of pure-dust soils is never less than  $\sim 80\%$  in the case of 1–3  $\mu\text{m}$  dust, and  $\sim 60\%$  in the case of crushed JSC Mars-1.

As expected for a constant experimental value of  $D_{12}$ , the behavior of the obstruction factor follows that of the diffusion coefficient. The increase in overall porosity toward pure dust demands that the degree of convolution of the pore geometry become larger to account for the decreasing diffusion coefficient. This is facilitated at lower dust contents in the case of crushed JSC Mars-1 by the broad particle size range. Dust composed only of micron-sized particles does not begin to have an appreciable effect on the pore geometry until its mass fraction is substantially higher. However, the implied increase in tortuosity may not occur for some micron-sized dust mixtures since it has been shown that the diffusion coefficient of uncompact pure micron dust is *higher* than that of any observed mixture. The low bulk density of the dust, the roughly equivalent particle sizes, and the angular particle shapes prevents closer packing and greater degrees of obstruction. Only mechanical compression (or dispersal and settling in a dense lubricating medium such as water) would further reduce the observed diffusivity, thereby increasing tortuosity.

To determine a tortuosity for each of these simulants and track how their structures change with dust content, porosimetry measurements of additional samples would be needed. Increasing pressure so as to measure the diffusivity in a purely Fickian regime (and thus be able to use equation (2.3)) becomes difficult as the smallest pore sizes reach the scale of microns. The pore size distribution measurements have indicated that particle size mixtures can either reduce the availability of large pore spaces (*i.e.* Mixture Type 1–A) or greatly enhance the number and size of the largest pores (*i.e.* Mixture Type 2–A). For JSC Mars-1 and mixtures of glass beads with fines, the pore distributions measured were broad. According to the results of *Clifford and Hillel* (1983, 1986), who show that larger pore spaces accommodate a majority of the flux, even a high proportion of pore spaces experiencing significant numbers of molecule-wall collisions should be less significant to the

overall diffusion rate than the few large pathways which may be open in an uncompacted, dust-rich structure. Thus, a real soil may have many pore spaces which experience primarily Knudsen-type diffusion under Mars surface conditions, but a small proportion of large pores undergoing significantly Fickian diffusion may dominate the vapor flux.

Aeolian processes can be efficient at sorting particles, resulting in particle assemblages which consist mainly of grains of similar size. Wind ripples such as those in Meridiani Planum show a small scale variation in the size of surface particles, but the interiors of the ripples are composed of grains on the order of 50–200  $\mu\text{m}$  (*Sullivan et al.*, 2005). Given the ubiquitous presence of micron-sized dust, and its tendency to adhere to solid surfaces, it is highly likely that some fraction of dust is incorporated into the soil. Dustier locales than Meridiani Planum may exhibit even higher concentrations of fines. However, the results presented here suggest that the diffusive properties of Mars soils will not be greatly affected by the presence of moderate amounts of micron-sized dust. Moreover, soils composed primarily of dust may exhibit the highest diffusivities. This conclusion, combined with the large specific surface areas for adsorption and expected large porosities of dusty deposits, supports the notion that dusty regions on Mars are significant components of past and present-day water cycles and are not isolated from the atmosphere.

The probability that an otherwise homogeneous layer of diffusive material will contain a crack or other efficient path to vapor transport will scale with the area considered. Such pathways may be caused by thermal cycling, micro-tectonic phenomena, slumping, or (in areas where possible) wetting and drying effects. The samples observed in this controlled laboratory environment are relatively small and are not generally subject to phenomena which cause cracking. However in certain cases where the material exhibited a moderate degree of cohesiveness (*e.g.*, pure dusts or mixtures incorporating crushed JSC Mars-1) cracking was initiated by slumping into the void left by sublimating ice. Sudden changes in mass loss rate, as would be expected if the crack extended from the surface to the ice, were not observed.

On Mars, such internal deformations of poorly to moderately cohesive regoliths may prevent cracking on the scale of millimeters from affecting the loss rate of ice which is several centimeters beneath the soil surface. If the material were highly cohesive a crack may penetrate deeply and remain unfilled, resulting in a locally depleted ice layer. The radius of influence of the crack will depend on the mechanical properties of the surrounding soil and whether the crack reaches the ice table.

#### 4.5.6 Implications

The samples studied cover a wide range of particle size distributions, porosities, and salt contents. Yet in no case has more than an order of magnitude reduction in fluxes or simulant diffusivity been observed. At most, the diffusivity of the baseline soil simulant (50–80  $\mu\text{m}$  glass beads) has been

reduced by a factor of about 8, with more common reductions being a factor of 2–3. Magnesium sulfate salt produces a moderate reduction at low salt concentrations, but has its greatest effect above 10 wt%. Mixtures of coarse and fine particles can produce a decreased diffusion coefficient (as for crushed JSC Mars-1) or no observable effect (as for 1–3  $\mu\text{m}$  dust). Mechanical packing of pure dust samples results in a reduction in diffusivity by a factor of 4–8. Overall, regolith materials similar to the simulants studied should not be expected to reduce the transport of water vapor by much more than an order of magnitude. The mechanism of formation of a diffusive barrier is significant in determining the degree of restriction.

Dust and larger particles could be incorporated into ice-rich deposits in a variety of ways, and these dirty ices could then produce lags upon ice sublimation. Two examples of sublimation lags can be considered: mid-latitude glaciers and polar layered deposits. For mid-latitude glaciers to persist under climate conditions similar to the present for timescales comparable to obliquity variations, they would need to be buried beneath a lag of order tens of meters or more.

Polar layered terrain is composed of alternating bright and dark layers which are interpreted as relatively dust-poor and dust-rich deposits, respectively. The layering is believed to be tied to climate cycles and sequential eras of precipitation and sublimation. The dust in the layers may either be deposited contemporaneously with the ice, or could be emplaced as part of cyclical global dust storms. In both cases, the dust which collects to form the lag would not be subject to compaction forces until the next period of ice deposition. Sublimation during an ice-loss phase would build a lag of uncompressed micron-sized dust particles. If such a lag does not become thick enough to exhibit self-compaction (possibly on the order of a few decimeters), these experiments show that such an uncompressed material would not reduce surface fluxes of water vapor by more than an order of magnitude relative to unprotected ice at the same temperature (see Figure 3.10). Additionally, the amount of dust deposited with the ice would have to be significant to build up a monolayer of dust after the sublimation of meters of ice. Recent observations by subsurface radar sounding instruments estimate an impurity content ranging from 2–15% for the North and South Polar Layered Deposits (*Picardi et al.*, 2005; *Plaut et al.*, 2007), consistent with gravity and topography inversions for density (*Zuber et al.*, 2007).

The diffusivity of a given deposit can be estimated from remote observations as well as geologic and geomorphic contextual information. By considering the context as well as remote or *in situ* observables, three quantities which feed into porosity and tortuosity estimations: the dust content, degree of compaction, and grain size distribution, may be constrained. The results obtained may be used along with homogeneous media diffusion quantities in subsequent models of complex regoliths by adding the contributions of layers with relatively higher or lower dust contents in series.

All observations of salt-bearing and salt-encrusted soils on Mars have thus far been made at low-latitude sites where there is no buried ice. As yet there are no *in situ* observations of soil

mechanical and geometric properties from a site known to overly subsurface ice. The Phoenix lander could perform the first such observations. Trenching activities will also be reveal the presence of a cohesive surface layer if one exists. Chemical experiments performed by the MECA instrument's Wet Chemistry Lab will probe the type and amount of soluble salt component in the soil and the contribution of this salt to the diffusive barrier may be interpreted in light of the laboratory experiments presented.